



Cyclic flexural response and energy dissipation of cold-formed steel framing members



David A. Padilla-Llano*, Matthew R. Eatherton, Cristopher D. Moen

The Charles E. Via, Jr. Dept. of Civil & Environmental Engineering, Virginia Polytechnic Institute and State University, 200 Patton Hall, Blacksburg, VA 24061, USA

ARTICLE INFO

Article history:

Received 10 October 2014

Received in revised form

20 October 2015

Accepted 21 October 2015

Available online 28 October 2015

Keywords:

Cold-formed steel

Seismic behavior

Energy dissipation

Moment-rotation behavior

Buckling

Thin-walled

Flexural response

ABSTRACT

This manuscript summarizes an experimental program investigating the cyclic flexural behavior and energy dissipation of C-shaped cold-formed steel structural framing members experiencing global, distortional or local buckling. Understanding the cyclic flexural moment-rotation ($M-\theta$) response of individual members is essential in developing analytical models that can facilitate analysis-based design of cold-formed steel building systems. Specimen cross-section dimensions and lengths were selected to isolate specific buckling modes (i.e., local, distortional or global buckling). A cyclic loading protocol was adapted from FEMA 461 with targets based on elastic buckling properties. Abrupt drops in flexural strength after peak moment were observed with subsequent stiffness degradation and pinching of the moment-rotation response associated with straightening of buckling deformations during loading direction reversals. Members experiencing local and distortional buckling accumulated damage at the compressed web and flanges within the leading buckled half-wave that spread throughout the cross-section forming flexural hinges after several cycles. In members experiencing lateral-torsional buckling, damage localized at the C-section flange-stiffening lip but distinct flexural hinges were not observed. Energy dissipation per cycle in members undergoing lateral-torsional buckling remained constant through large flexural rotations because the failure mechanism involved mid-span cross-section rigid body motion without plastic deformations spreading across the cross section. Local and distortional buckling specimens resulted in more dissipated energy per cycle compared to global buckling specimens, but the energy dissipation rapidly decreased as applied displacements increased. Energy dissipation within the damaged half-wave(s) is higher for lower cross-sectional slenderness and increasing section modulus, key trends that will be useful for generally defining cyclic hysteretic response of thin-walled cold-formed steel members in planned future work.

© 2015 Elsevier Ltd. All rights reserved.

1. Introduction

A shift is progressing in light steel framed building seismic design to analysis-based engineering which is motivating building seismic performance studies considering thin-walled behavior including buckling deformation and its role in strength and stiffness degradation. Research efforts towards a better understanding of CFS building seismic behavior have traditionally focused in sheathed or strapped shear wall studies (e.g., [1–12]); however the most recent research efforts grouped under the CFS-NEES project, seek to advance understanding in the seismic behavior of cold-formed steel buildings and the building blocks (e.g., members, connections, floor diaphragm, shear walls) for developing non-linear models and response history analysis [13]. These projects

include shear wall tests [4,5,10,11], sheathing to steel connection tests [14,15], moment-rotation response characterization considering local and distortional buckling [16], and the recently completed full scale CFS-NEES building shake table tests that quantified structural and non-structural subsystem contributions to whole building seismic response [17–19].

There is still a need to expand CFS seismic knowledge at the more basic levels, e.g., member cyclic behavior including buckling deformations, and how they contribute to building response (e.g., diaphragms, moment-frames and shear walls). Furthermore, to validate seismic performance factors (i.e., R , Ω_0 , and C_d) for design, considering different hazard levels that provide protection against collapse [20], it is necessary to analyze a wide range of building configurations subjected to suites of ground motions scaled to multiple intensity levels [21]. This in turn requires computationally efficient and accurate modeling tools to simulate the cyclic response and capture key response characteristics in CFS systems and components.

* Corresponding author.

E-mail address: dapadill@vt.edu (D.A. Padilla-Llano).

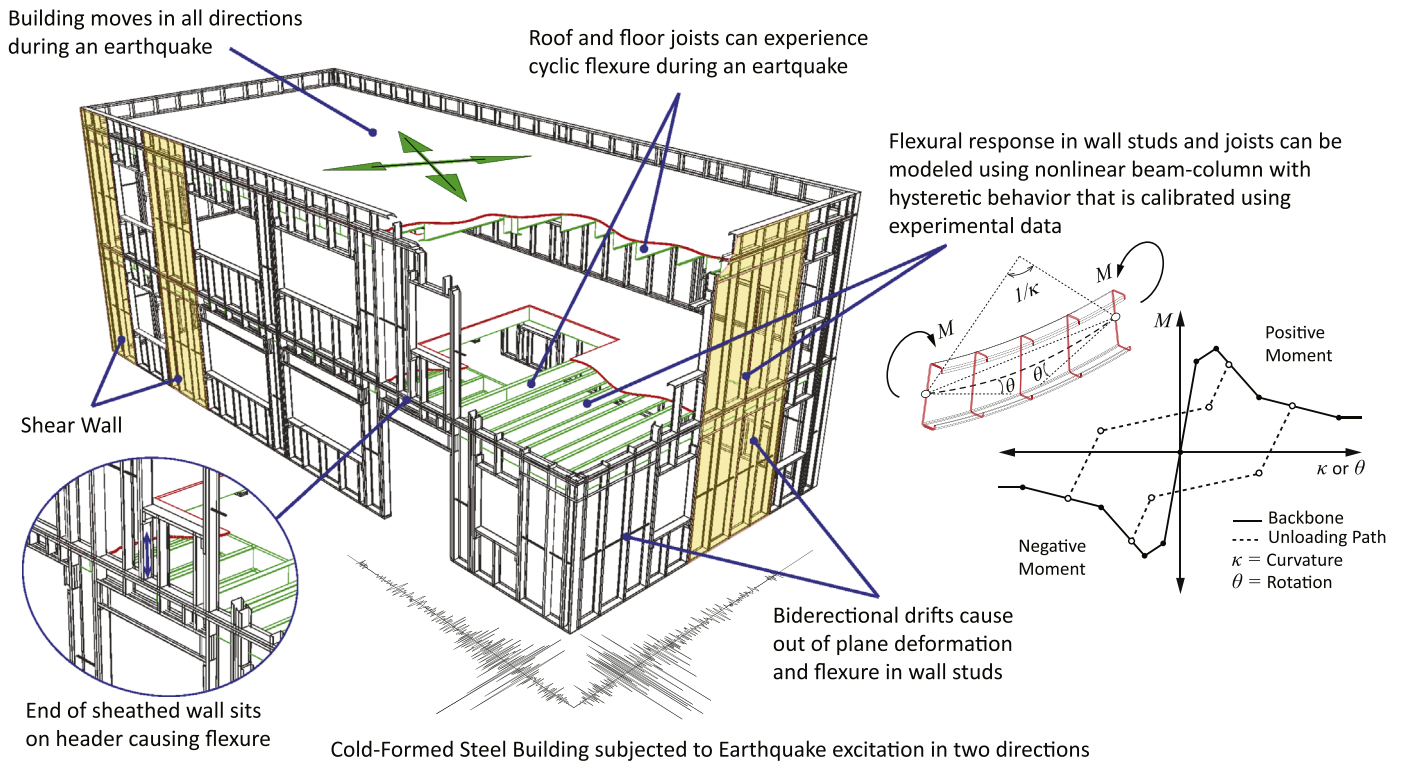


Fig. 1. Cold-formed steel framing experiences flexure during earthquake excitations (adapted from CFS-NEES building model [19]) with behavior that can be represented by phenomenological models [22].

Within this analysis-based framework, engineers and researchers will model a CFS framed building depicted in Fig. 1 using nonlinear beam-column or hysteretic spring models calibrated using cyclic experimental data (e.g. [22]). Developing such nonlinear models requires characterizing the cyclic behavior and energy dissipation in all these components. The research summarized in this manuscript addresses this need by experimentally investigating cyclic behavior and energy dissipation characteristics of cold-formed steel flexural members that experience lateral-torsional buckling, distortional buckling and local buckling deformations. This work complements the recently completed experimental program on CFS axial members (lipped-channel studs) cyclic behavior [23].

Existing research on cyclic behavior of cold-formed steel flexural members is scarce and primarily focuses on flexural response as part of bolted steel moment connections (e.g. [24–26]). Cyclic tests on hot-rolled steel I-beams experiencing global buckling (i.e., lateral-torsional buckling) demonstrated that strength deteriorates after buckling initiates with localized inelastic strains accumulating at the compression flange [27,28]. Strength decreases even more rapidly if flexure is combined with axial loading. Post-buckling strength degradation in thin-walled cold-formed steel I-beams that exhibited lateral-torsional buckling is more severe for stiffer members, and stiffness degradation was more severe for beams with lower flexural rigidity [29]. This suggests that there is a relationship between slenderness (member and cross-sectional) and cyclic performance, which was confirmed recently for axial CFS members [23] and is a key motivator for the flexural experiments presented in this manuscript.

Local buckling deformations define thin-walled member cyclic behavior. Experiments on steel circular and rectangular tubes under constant amplitude cyclic uniform bending showed that strength deteriorated from tube wall local buckling [30–32], and that performance of rectangular steel tubes deteriorated due to inelastic buckling deformations accumulation in the compression

face with collapse when kinks developed at the dominant local buckling half-wave [33]. More recent studies investigating energy dissipation associated with local buckling deformations in cold-formed steel beams subjected to constant amplitude cyclic bending [34–36] showed that strength degrades rapidly in the first cycles and reduces to an almost constant magnitude. This is a consequence of localized inelastic buckling deformations (and subsequent fracture) slowly spreading throughout the cross-section as number of cycles increased. Residual strength after several cycles can be beneficial in the context of collapse analysis and design of CFS systems.

With general hysteretic response characterization for CFS system modeling in mind, this paper summarizes an experimental program that investigated the cyclic behavior and energy dissipation of CFS flexural members with a focus on thin-walled buckling limit states. Specimen cross-section dimensions, unbraced lengths, and test boundary conditions were strategically selected to isolate thin-walled member buckling limit states common to open cross-section thin-walled CFS joists (i.e., lateral-torsional, distortional and local buckling). Strength and stiffness degradation were carefully documented, and trends related to cross-sectional slenderness and energy dissipation are discussed. The next section introduces the experimental program, specimen selection strategy, test setup and loading protocol.

2. Experimental program

An experimental program was conducted to study the cyclic behavior of CFS flexural members (lipped-channels without perforations) experiencing local, distortional and global buckling deformations. Specimens were subjected to four-point bending with a constant moment region of length L_u . Shear and axial (catenary) forces in the unbraced length (L_u) were prevented with custom designed test fixtures introduced in this section. The program

Table 1

Test matrix with nominal dimensions, number of tests, and displacement loading rate.

Specimen ^a	Buckling Limit ^b	L_u	H	B	t	No. of Cyclic Tests	No. of Monotonic Tests	Cyclic Disp. Rate	Monotonic Disp. Rate
		(mm)	(mm)	(mm)	(mm)			(mm/min)	
800S200-33-LF#	Local	1626	203	51	0.88	2	2	20.57	0.35
1000S200-43-LF#	$(\lambda_e, \lambda_d, \lambda_e)$	1626	254	51	1.15	2	2	30.85	0.52
800S250-68-DF#	Distortional	1626	203	64	1.81	2	2	28.55	0.48
1200S250-97-DF#	λ_d, λ_e and λ_e	1626	305	64	2.58	2	2	42.82	0.73
800S162-97-GF#	Global	3048	203	41	2.58	2	2	34.26	0.58
1200S162-97-GF#	λ_e, λ_e and λ_d	3048	305	41	2.58	2	2	42.82	0.73

^a F = Flexural, G = Global, D = Distortional, L = Local, # indicates Cyclic or Monotonic.^b λ_e , λ_d and λ_e = local, distortional and global slenderness parameter respectively [37].

included monotonic and cyclic tests where the monotonic tests served as a baseline moment-rotation response to quantify cyclic strength and stiffness degradation.

2.1. Specimen selection strategy

Specimen cross-sections and unbraced lengths, L_u , were selected such that their monotonic flexural strength was governed either by local, distortional or global buckling as predicted by the American Iron and Steel Institute (AISI) Direct Strength Method [37]. Six cross-sections were selected from standard sizes listed in the Structural Stud Manufacturers Association (SSMA) catalog [38] with web widths ranging from 203 to 305 mm and nominal thicknesses between 0.88 mm and 2.58 mm. Global buckling specimens had an unbraced length $L_u = 3048$ mm, while local and distortional buckling specimens had an unbraced length, $L_u = 1626$ mm. The test matrix is summarized in Table 1 (with nominal dimensions) and specimen nomenclature and cross-section variables are defined in Fig. 2.

2.2. Specimen dimensions, material properties and elastic buckling moments

Cross-section dimensions were measured at the member's mid-span using methods described in [39]. See Fig. 2b for definitions of measured quantities and Table 2 for values. The measured dimensions were input in the finite strip eigen-buckling analysis software CUFSM [40] to calculate the elastic buckling moment for local buckling, M_{crf} , distortional buckling, M_{crd} , and global buckling, M_{cre} , along with the associated half-wavelengths (L_{crf} , L_{crd} , and L_{cre} respectively). Warping, twist and minor axis flexure were assumed fixed at loading points when calculating the elastic

buckling moments, i.e., an effective length of $0.5 L_u$ was used when calculating M_{cre} . The yield moment, M_y , was determined using the cross-section moment of inertia (calculated using measured dimensions) at mid-span and the average measured yield stress, F_y , obtained from three coupon tests per specimen. Coupon tests were conducted in accordance with ASTM E8M-13a [41] with one coupon taken from each flange and one from the web. A typical stress-strain curve from a coupon test is shown in Fig. 3. The monotonic flexural capacities, M_n , were calculated using the AISI Direct Strength Method [37] and the values are summarized in Table 3.

2.3. Test setup and instrumentation

Tests were conducted in a four point bending configuration to produce constant moment along the unbraced length. All members span 4877 mm between end supports and are loaded through an adjustable spreader beam that accommodates variation in loading point location to change the unbraced length L_u (see Fig. 4). Loading attachments and end supports were detailed to allow rotation about the cross-section major bending axis. Slotted holes were used at the supports and at one of the loading points to prevent axial forces from developing in the specimen. Lateral braces were placed along the shear spans of length a , to develop longitudinal warping and minor axis flexure fixed conditions at the loading points that defined the unbraced length.

A cyclic displacement history was applied at the loading points using a customized control program receiving feedback from two vertical linear potentiometric transducers placed at the load points. A displacement rate was derived such that the strain rate at the extreme fiber remained constant at 0.002 mm/mm/min. Based on monotonic tension coupon tests described in the literature, this

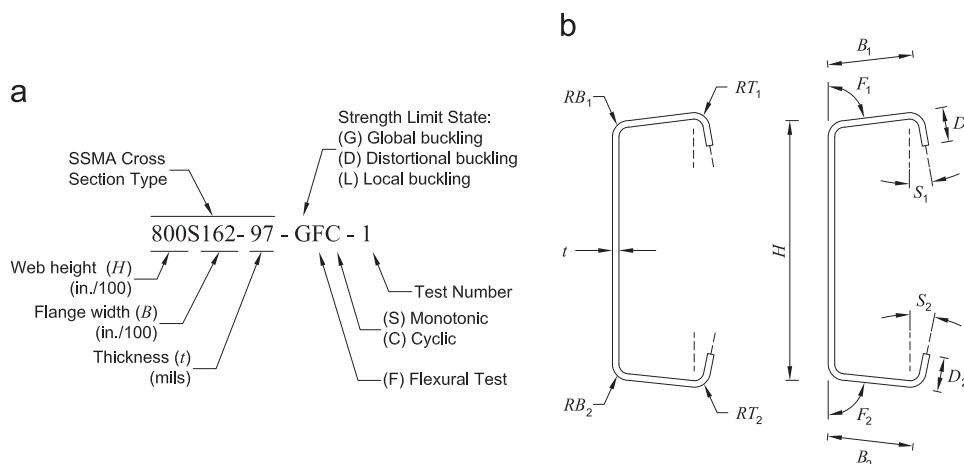
**Fig. 2.** Test specimen (a) naming convention; and (b) cross-section dimension nomenclature.

Table 2
Measured specimen dimensions.

Specimen	<i>L</i>	<i>A_g</i> ^a	<i>I_x</i> ^a	<i>D₁</i>	<i>D₂</i>	<i>B₁</i>	<i>B₂</i>	<i>H</i>	<i>RT₁</i>	<i>RB₁</i>	<i>RT₂</i>	<i>RB₂</i>	<i>F₁</i>	<i>F₂</i>	<i>S₁</i>	<i>S₂</i>	<i>t</i>
	(mm)	(mm ²)	(cm ⁴)	(mm)	(mm)	(mm)	(mm)	(mm)	(mm)	(mm)	(mm)	(mm)	(°)	(°)	(°)	(°)	(mm)
1200S162-97-GFC-1	3048	995	1111	9.8	11.3	42.5	43.1	305.7	4.8	5.6	5.2	5.6	91.2	88.0	−2.8	2.6	2.52
1200S162-97-GFC-2	3048	993	1111	10.1	10.9	42.8	43.1	305.7	5.0	5.6	5.2	5.6	90.9	87.5	−2.8	3.0	2.51
1200S162-97-GFM-1	3048	991	1105	10.0	11.1	42.3	43.2	305.9	4.8	5.6	5.2	5.6	91.2	88.2	−3.7	−3.1	2.51
1200S162-97-GFM-2	3048	992	1104	10.8	10.0	42.8	42.0	305.7	5.2	5.6	4.8	5.6	88.7	90.7	2.5	−4.0	2.52
800S162-97-GFC-1	3048	734	400	9.7	11.4	42.9	42.5	203.9	4.4	5.6	5.2	5.2	90.6	88.8	−2.3	0.7	2.50
800S162-97-GFC-2	3048	734	398	12.4	13.0	40.6	40.2	203.9	5.0	5.4	5.2	5.4	90.3	88.8	0.5	2.1	2.50
800S162-97-GFM-1	3048	732	398	9.9	11.4	42.4	42.3	204.0	4.8	5.4	5.2	5.2	90.6	88.8	−2.7	−1.1	2.50
800S162-97-GFM-2	3048	735	400	12.2	13.6	40.3	39.9	203.8	4.8	5.4	5.2	5.2	89.0	87.7	0.7	2.1	2.51
1200S250-97-DFC-1	1626	1148	1427	12.9	14.5	65.8	64.9	306.6	5.2	5.6	5.6	5.6	92.2	89.8	−4.2	−3.7	2.57
1200S250-97-DFC-2	1626	1140	1421	12.6	14.5	65.1	65.7	306.5	5.2	5.6	5.6	5.6	91.4	89.5	−4.0	−4.1	2.56
1200S250-97-DFM-1	1626	1154	1437	12.7	14.7	65.7	65.9	306.8	5.2	5.6	5.6	5.6	92.7	89.5	−5.3	−2.9	2.58
1200S250-97-DFM-2	1626	1148	1434	12.8	14.7	66.0	66.4	306.8	5.2	5.6	5.6	5.6	92.0	89.7	−4.6	−5.7	2.56
800S250-68-DFC-1	1626	618	377	12.2	14.2	63.2	64.4	204.2	4.0	4.0	4.2	4.6	91.9	89.3	−5.3	−5.0	1.79
800S250-68-DFC-2	1626	615	373	14.6	11.5	63.8	63.0	204.2	8.7	4.8	4.2	4.0	90.6	90.5	−4.1	−4.1	1.80
800S250-68-DFM-1	1626	623	378	14.2	12.4	63.8	63.8	204.3	4.4	4.8	4.0	4.0	91.7	91.0	−3.2	−3.8	1.81
800S250-68-DFM-2	1626	625	382	14.4	12.1	65.0	63.7	204.1	4.4	4.4	4.2	4.0	90.6	90.6	−4.6	−4.1	1.81
1000S200-43-LFC-1	1626	418	360	10.2	11.8	49.2	50.3	254.0	3.6	3.2	3.6	3.6	89.6	87.0	1.0	0.9	1.14
1000S200-43-LFC-2	1626	422	364	10.3	12.0	49.1	50.1	254.4	3.6	3.2	3.6	3.6	90.5	86.8	0.7	2.0	1.15
1000S200-43-LFM-1	1626	422	364	10.3	12.0	49.2	50.2	254.5	3.6	3.2	3.6	3.6	90.4	87.4	0.2	1.1	1.15
1000S200-43-LFM-2	1626	424	365	10.1	12.0	49.2	50.3	254.4	3.6	3.2	3.6	3.6	90.8	87.2	0.3	1.5	1.16
800S200-33-LFC-1	1626	285	168	14.5	14.7	49.9	49.9	204.7	3.6	3.2	3.6	3.2	90.7	90.6	1.9	0.1	0.88
800S200-33-LFC-2	1626	302	178	14.0	14.1	52.8	50.2	203.7	3.6	3.2	4.4	3.2	90.1	90.5	−0.7	1.0	0.93
800S200-33-LFM-1	1626	286	169	14.5	15.2	49.5	49.9	204.5	3.6	3.2	3.6	3.2	91.5	88.9	−1.7	1.1	0.88
800S200-33-LFM-2	1626	287	170	14.7	14.7	50.0	49.3	204.7	3.6	3.0	3.6	3.4	90.7	89.6	−0.8	−0.2	0.88

^a Calculated from measured geometry, see the dimension definitions in Fig. 2.

displacement rate is expected to produce yield stresses approximately 2% larger than the static yield stress [43]. The displacement rate for the monotonic tests was derived based on a constant strain rate at the extreme fiber of 0.00003 mm/mm/min, which corresponds to 1/3 of the maximum rate of 21 MPa per minute recommended in the AISI test method for flexural testing of cold-formed steel beams [44]. The derived displacement rates applied at the loading points for each type of specimen are listed in Table 1.

2.4. Displacement-controlled testing protocol

The displacement-controlled testing protocol (see Fig. 5) is adapted from the FEMA 461 quasi-static cyclic deformation-controlled testing protocol. The FEMA 461 protocol was developed to obtain fragility data and hysteretic response characteristics of

building components for which damage is best predicted by imposed deformations [45]. CFS flexural members can experience symmetrical or asymmetrical loading depending on the end connections (e.g., screwed or welded connection), bracing conditions, and location within a building system (e.g., floor joist compared to a stud in a shear wall). The adapted protocol is fully reversed with symmetric displacement amplitudes. The loading protocol comprises steps of increasing amplitude with two cycles per step. Each step's displacement amplitude is 40% larger than the previous, i.e. $\delta_i = 1.4\delta_{i-1}$ (see Fig. 5). The loading protocol is anchored to the elastic displacement, $\delta_e = M_e a(3L_u + 2a)/6EI$ (EI =elastic bending stiffness), at the fourth step (i.e., 7th and 8th cycles). The moment associated with stiffness degradation from buckling deformations, M_e , is estimated using slenderness limits defined in the AISI Direct Strength Method (DSM) [37]. The DSM approach predicts that local buckling initiates at $\lambda_{\ell} = 0.776$ and distortional buckling initiates at $\lambda_d = 0.673$. Calculating the slenderness $\lambda = (M_e/M_{cr})^{0.5}$, the moments associated with stiffness degradation from buckling deformations are $M_e = 0.60M_{cr\ell}$ and $M_e = 0.45M_{crd}$ for local and distortional buckling respectively. The DSM approach estimates that global buckling deformations initiate at $M_e = 0.36M_{cre}$. Elastic displacements, δ_e , are listed in Table 3 for all specimens.

2.5. Specimen imperfections

Initial geometric imperfections in CFS members reduce flexural strength and initial stiffness. The predicted strength decreases the most if the imperfections resemble the governing buckling modes [39,46,47]. Member imperfections are defined as the specimen geometry deviations from the straight “perfect” member before attaching it to the supports (see Fig. 6). Imperfections were measured and characterized using methods described in [48].

The average global sweep imperfections δ_B in distortional and local buckling specimens (short members) were smaller than the tolerance limits given in ASTM C955-09 [49] as shown in Table 4. For global buckling specimens (long members), the average sweep δ_B was larger than the ASTM limit of $L/960$ leading to measured

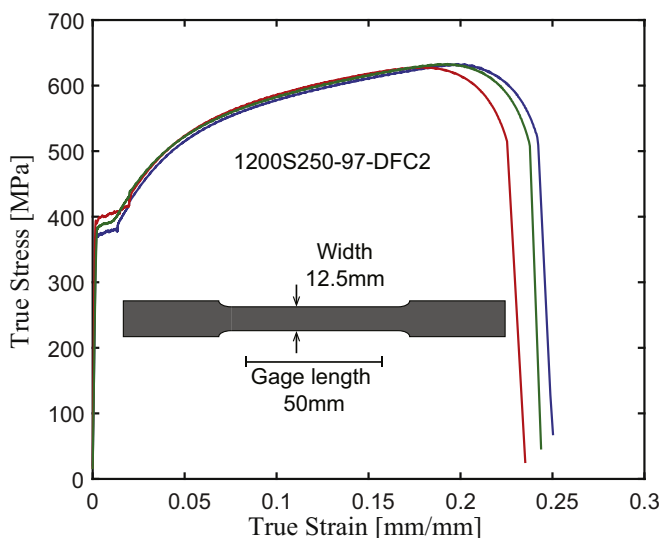


Fig. 3. Typical stress-strain curve from coupon tests.

Table 3
Elastic buckling properties and predicted flexural strength.

Specimen	F_y^a	F_u^a	M_y	M_n^b	M_{cre}	λ_e^c	M_{crd}	λ_d^c	L_{crd}	$M_{cr\ell}$	λ_{ℓ}^c	$L_{cr\ell}$	δ_e
	(MPa)			(kN-mm)			(kN-mm)		(mm)	(kN-mm)		(mm)	($\times 10^{-3}$ mm)
1200S162-97-GFC-1	448	574	32664	15524 (11435)	15524	1.45	23387	1.18	252	28195	0.74	141	3871
1200S162-97-GFC-2	464	575	33835	15835 (11689)	15835	1.46	23557	1.20	254	28379	0.75	141	3951
1200S162-97-GFM-1	451	566	32668	15272 (11296)	15272	1.46	23276	1.18	252	28028	0.74	141	3830
1200S162-97-GFM-2	440	568	31850	16530 (11986)	16530	1.39	24544	1.14	260	29561	0.75	139	4149
800S162-97-GFC-1	452	578	17786	10005 (7416)	10006	1.33	24668	0.85	221	34810	0.54	92	6937
800S162-97-GFC-2	454	575	17752	9854 (7393)	9854	1.34	27939	0.80	249	36219	0.52	92	6867
800S162-97-GFM-1	452	579	17711	9721 (7261)	9721	1.35	24901	0.84	220	34704	0.53	92	6770
800S162-97-GFM-2	462	580	18182	9623 (7274)	9623	1.37	27902	0.81	244	36195	0.52	92	6664
1200S250-97-DFC-1	411	537	38450	27721	208449	0.43	31050	1.11	376	39466	0.99	141	10537
1200S250-97-DFC-2	385	531	35914	26249	199162	0.42	30076	1.09	367	38276	0.97	141	10255
1200S250-97-DFM-1	389	530	36673	26845	206543	0.42	30839	1.09	370	39349	0.97	141	10393
1200S250-97-DFM-2	404	532	37977	27340	208425	0.43	30546	1.12	375	38865	0.99	141	10316
800S250-68-DFC-1	385	466	14292	10247	81992	0.42	11373	1.12	410	15650	0.96	117	14595
800S250-68-DFC-2	377	462	13833	10575	82729	0.41	13084	1.03	451	16544	0.91	113	16995
800S250-68-DFM-1	376	465	14007	10658	88723	0.40	13079	1.03	462	16680	0.92	113	16739
800S250-68-DFM-2	377	464	14148	10719	91237	0.39	13057	1.04	469	17022	0.91	113	16570
1000S200-43-LFC-1	424	478	12034	6056	36445	0.57	3997	1.74	363	3378	1.89	139	6037
1000S200-43-LFC-2	421	476	12047	6125	36989	0.57	4098	1.71	365	3443	1.87	139	6098
1000S200-43-LFM-1	418	479	11983	6114	37083	0.57	4110	1.71	365	3454	1.86	139	6111
1000S200-43-LFM-2	419	476	12045	6090	36932	0.57	4045	1.73	358	3468	1.86	140	6123
800S200-33-LFC-1	335	403	5550	3197	26252	0.46	3136	1.33	582	1797	1.76	109	6881
800S200-33-LFC-2	307	371	5377	3358	30191	0.42	3417	1.25	578	2184	1.57	109	7907
800S200-33-LFM-1	335	404	5575	3208	25679	0.47	3190	1.32	575	1799	1.76	110	6858
800S200-33-LFM-2	337	405	5632	3257	26365	0.46	3257	1.31	586	1843	1.75	109	7001

^a F_y , F_u =yielding and ultimate stresses respectively measured from coupon tests.

^b M_n =predicted moment capacity using AISI-S100-12 [37], values in parentheses are predicted capacity using Eurocode 3 [42].

^c $\lambda_e=(M_y/M_{cre})^{0.5}$; $\lambda_d=(M_y/M_{crd})^{0.5}$; $\lambda_{\ell}=(M_{ne}/M_{cr\ell})^{0.5}$; M_{ne} =predicted flexural capacity for lateral-torsional buckling.

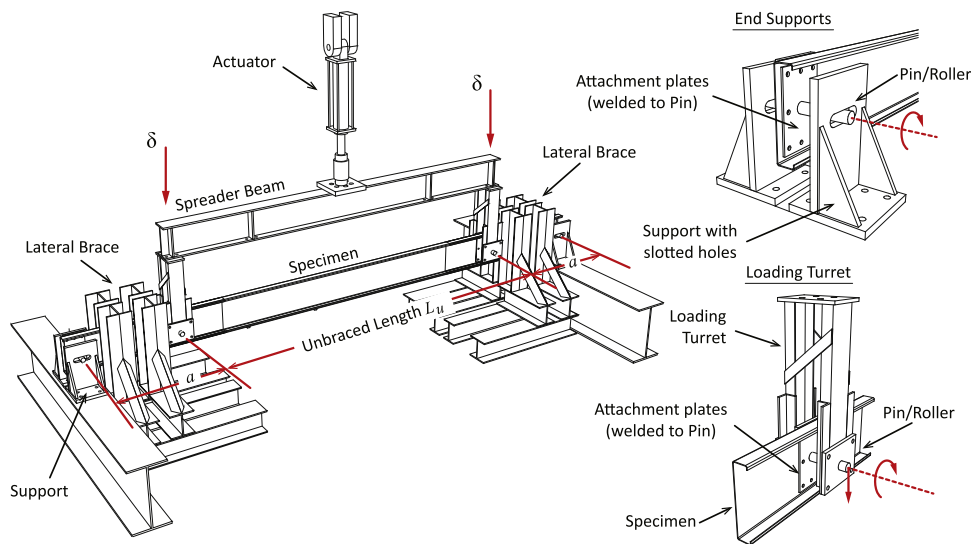


Fig. 4. Test setup with support and loading details.

flexural strengths, M_{max} , less than the predicted, M_n (see Section 3.1). Global buckling specimens ($L_u=3048$ mm) with the highest thickness $t=2.51$ mm have the largest sweep imperfections. Imperfection magnitudes in CFS members are known to increase with sheet thickness because of plastic strains and associated residual curvature caused by coiling the sheet for transportation and manufacturing [50,47]. Out-of-straightness in the strong axis direction, δ_c , was smaller than the ASTM limits for all specimens. Local imperfections were also all lower than ASTM limits and smaller than $\delta_w/t=1.35$ and $\delta_f/t=3.44$ associated with occurrence probabilities $P(\delta < \delta_w)=0.95$ and $P(\delta < \delta_f)=0.95$ defined in [51]. A detailed discussion about the measured imperfections and their characterization from this testing program can be found in [48].

3. Experimental Results

Moment-rotation ($M-\theta$) responses were obtained for all specimens. Experimental values for rotation, $\theta=\delta/a$, were calculated as the average displacement measured at the loading points, δ , divided by the shear span, a . This approximation yields more consistent measurements of the specimen's deformation at the loading points throughout the whole test than measuring rotations or curvature. Before the peak moment, rotations and curvature are continuous along the specimen's length, and equal right before (shear span side) and after (constant moment region side) the loading points. Once the peak moment is reached, both rotations and curvature are not necessarily continuous at the loading

points because of buckling deformations making these quantities less adequate for characterizing the response. The approximation is also consistent with lumped-spring models for CFS flexural members, e.g. [52]. Rotations are normalized to the yield rotation,

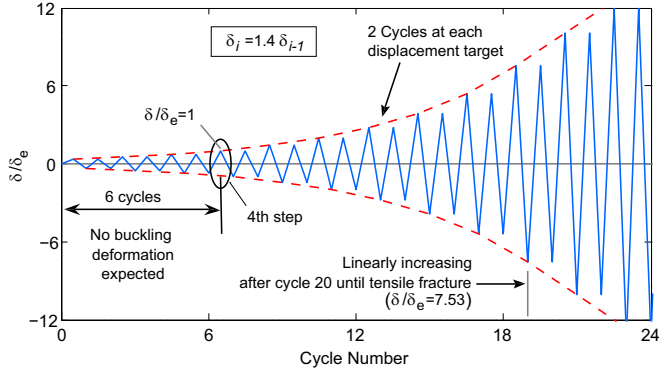


Fig. 5. Cyclic flexural cold-formed steel loading protocol.

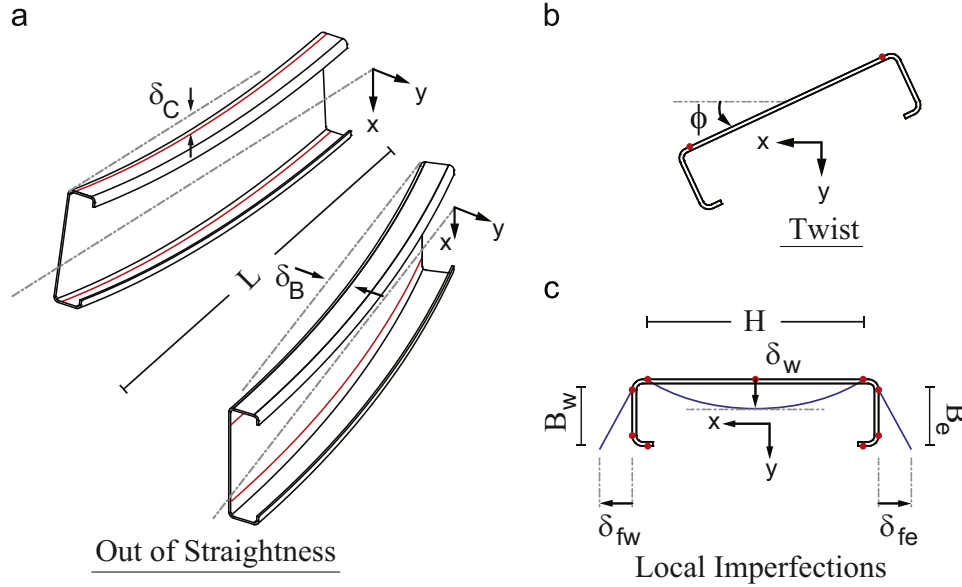


Fig. 6. Member imperfections: (a) global out-of-straightness (sweep); (b) initial twist; and (c) local web and flange imperfections.

Table 4

Test specimen measured imperfections statistics.

Specimen group		δ_B/L ($\times 10^{-3}$)		δ_C/L ($\times 10^{-3}$)		ϕ ($^\circ$)	δ_W/H ($\times 10^{-3}$)		δ_{FE}/B_e ($\times 10^{-3}$)		δ_{FW}/B_w ($\times 10^{-3}$)	
Global	Mean	1.45	(L/689)	0.37	(L/2710)	0.49	2.25	(H/444)	33.55	(B/30)	55.78	(B/18)
	Max	2.02	(L/495)	0.63	(L/1570)	0.64	2.84	(H/352)	60.13	(B/17)	66.30	(B/15)
	Min	1.01	(L/986)	0.15	(L/6770)	0.32	1.67	(H/600)	17.59	(B/57)	35.88	(B/28)
	St.Dev	0.52		0.25		0.16	0.59		23.17		17.24	
	COV	0.36		0.67		0.34	0.26		0.69		0.31	
Distortional	Mean	0.12	(L/8250)	0.35	(L/2880)	0.29	2.60	(H/385)	16.31	(B/61)	20.51	(B/49)
	Max	0.17	(L/5940)	0.55	(L/1820)	0.51	3.67	(H/272)	22.49	(B/44)	31.69	(B/32)
	Min	0.09	(L/11500)	0.16	(L/6370)	0.08	1.80	(H/557)	11.27	(B/89)	13.70	(B/73)
	St.Dev	0.04		0.16		0.19	0.93		4.74		8.01	
	COV	0.29		0.47		0.67	0.36		0.29		0.39	
Local	Mean	0.24	(L/4130)	0.29	(L/3500)	0.29	4.87	(H/205)	23.66	(B/42)	28.21	(B/35)
	Max	0.44	(L/2260)	0.46	(L/2200)	0.45	5.30	(H/189)	26.78	(B/37)	33.77	(B/30)
	Min	0.12	(L/8420)	0.18	(L/5630)	0.21	4.32	(H/231)	19.96	(B/50)	20.66	(B/48)
	St.Dev	0.14		0.12		0.11	0.42		3.39		6.29	
	COV	0.59		0.42		0.39	0.09		0.14		0.22	
ASTM C955 Tol.		L/960		L/960		L/H/384	1.59 mm (max)		1.59 mm (max)		1.59 mm (max)	

See imperfection definition in Fig. 5.

$\theta_y = \delta_y/a$, [$\delta_y = M_y a(3L_u + 2a)/6EI$], which corresponds to the yield moment $M_y = SF_y$ (S is the elastic section modulus). Experimental values of the moment are calculated as $M = aP$, where P is half of the measured vertical load. Positive moment and rotations correspond to downward loading and the negative values correspond to upward loading.

The loading protocol was continued to the maximum stroke of the hydraulic actuator or until the distance available to slide at the supports was expended. All members were deformed to a maximum downward/upward displacement of at least 63 mm. The following sections describe details of the monotonic and cyclic tests for each buckling limit state. Test videos are available in Virginia Tech's digital repository [53].

3.1. Monotonic flexural response

Monotonic flexural responses of members that experienced global (GFM), distortional (DFM), and local (LFM) buckling are shown in Fig. 7. The pre-peak responses are linear past 50% of the peak moment for all members and became nonlinear when

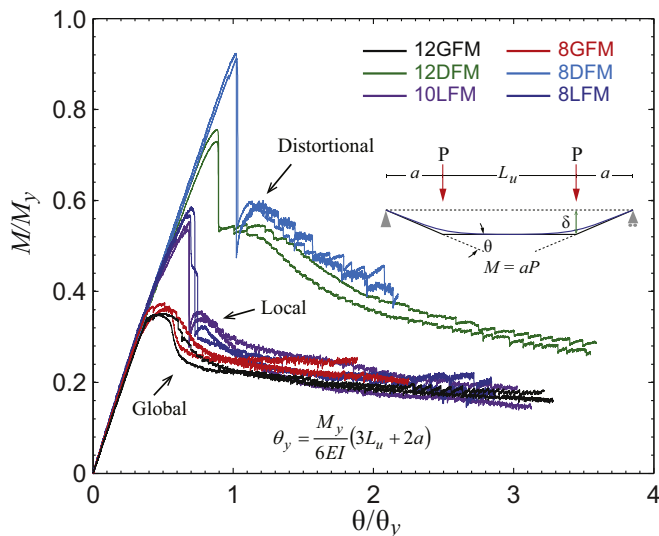


Fig. 7. Monotonic flexural responses normalized to the yield moment and rotation. Flexural capacity and post-peak response are least affected by buckling deformations for specimens 8DFM and 12DFM.

buckling deformations appeared. Buckling in all members started before the peak moment and cross-section failure happened close to the mid-span (see Fig. 8), with the exception of specimen 8DFM-2 where failure occurred half way between the mid-span and loading point; however, the moment-rotation behavior was still consistent with the other specimen in the group, 8DFM-1.

The average ratio of measured peak moment to predicted nominal capacity M_{max}/M_n was 0.96 with a coefficient of variation (COV) of 0.21 for all monotonic tests (see Tables 5 and 6). When considering only local and distortional buckling specimens, the average test-to-predicted moment ratio is 1.09 and coefficient of variation is 0.08 (see Tables 5 and 6) while for global buckling the

test-to-predicted mean was 0.70. The low test-to-predicted M_{max}/M_n ratios for global buckling specimens resulted from large sweep imperfections on average of $L/767$ coupled with the un-conservative AISI code treatment (e.g., AISI-S100-12 Section C.3.1.2.1 or Appendix 1.2.2.1, [37]) that equates the capacity to the critical elastic buckling moment without consideration of initial imperfections. If M_n is calculated using Eurocode-3, which include an imperfection factor $\alpha=0.49$ for lateral-torsional buckling [42], the average M_{max}/M_n ratio for global buckling members becomes 0.94 with a COV=0.04 (see Tables 3,5 and 6).

The measured initial stiffness k is not influenced by imperfections for all specimens as the average test-to-predicted stiffness ratio k/k_e was 0.95 (COV=0.04), with the global buckling specimens showing the lowest average $k/k_e=0.93$ (COV=0.04), see Tables 5 and 6. With these statistics the member initial stiffness is shown to be accurately characterized by $k_e = 6EI/(3L_u + 2a)$.

3.2. Flexural members experiencing global buckling (GFM)

Global buckling flexural members (GFM) exhibited lateral-torsional buckling deformation that started before the maximum flexural strength M_{max} , see Fig. 8a. At peak moment, the top flange at the intersection with the stiffening lip experienced inelastic local buckling and strength dropped rapidly to about 70% of the peak-moment. The moment-rotation response stabilized around $0.2 M_y$ for both cross-section types (Fig. 7). Even though the top flanges buckled and did not contribute to the flexural-torsional stiffness, the member was still able to carry load for large deformations because the web and web-flange intersections maintained their shape without plastic deformations spreading across the cross section. Inelastic deformations developed close to the loading points as the second hinge formed in the later test stages.

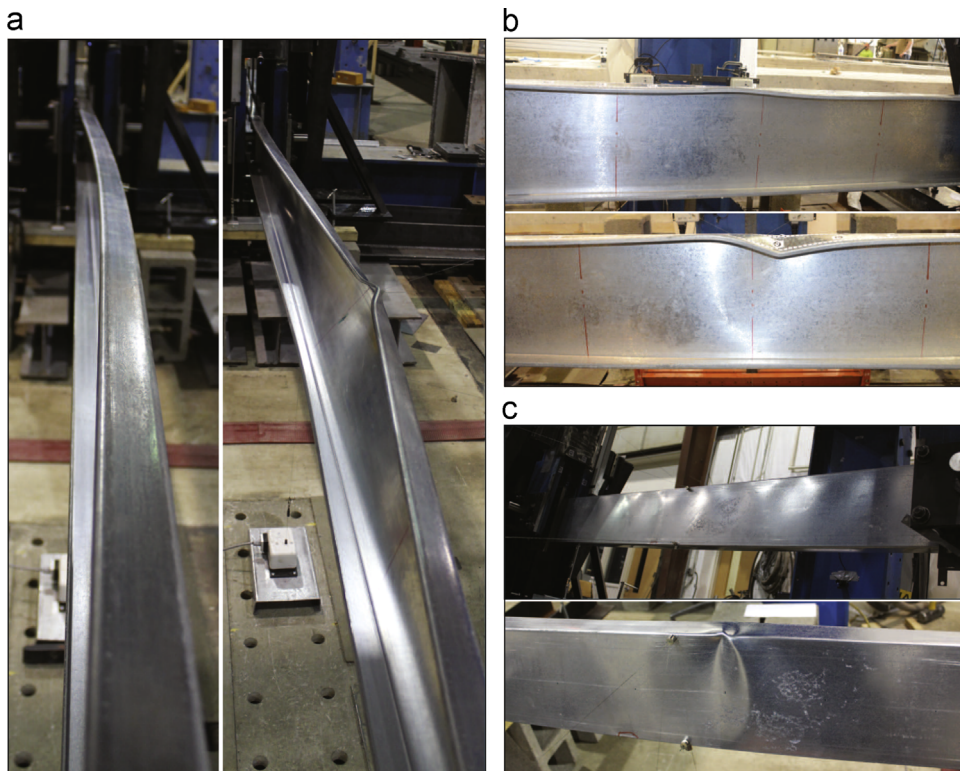


Fig. 8. Flexural buckling modes observed in the tests: (a) lateral-torsional buckling; (b) distortional buckling; (c) local buckling.

Table 5

As tested peak moments, rotations, and initial stiffness.

Specimen	M_{max}^a	M_{min}^a	θ_{Mmax}^a	θ_{Mmin}^a	θ_y	k_e^b	k^b	M_{max}/M_n^c	M_{min}/M_n^c	θ_{Mmax}/θ_y	θ_{Mmin}/θ_y	k/k_e
	(kN-mm)		($\times 10^{-3}$ rad)			(kN-m/rad)						
1200S162-97-GFC-1	10290	–10450	13	–13	27	1200	1050	0.66 (0.9)	0.67 (0.91)	0.48	–0.48	0.87
1200S162-97-GFC-2	11270	–11255	12	–11	28	1200	1065	0.71 (0.96)	0.71 (0.96)	0.42	–0.38	0.89
1200S162-97-GFM-1	11505		13	–	27	1195	1075	0.75 (1.02)	–	0.47	–	0.90
1200S162-97-GFM-2	11305		14	–	27	1190	1085	0.68 (0.94)	–	0.52	–	0.91
800S162-97-GFC-1	6905	–6630	20	–20	41	430	415	0.69 (0.93)	0.66 (0.89)	0.50	–0.50	0.97
800S162-97-GFC-2	7065	–6775	21	–20	41	430	415	0.72 (0.96)	0.69 (0.92)	0.50	–0.48	0.97
800S162-97-GFM-1	6500		21	–	41	430	415	0.67 (0.9)	–	0.51	–	0.96
800S162-97-GFM-2	6905		21	–	42	430	420	0.72 (0.95)	–	0.50	–	0.97
1200S250-97-DFC-1	28505	–29080	17	–16	19	2060	1940	1.03	1.05	0.91	–0.85	0.94
1200S250-97-DFC-2	28120	–28590	16	–16	18	2050	1900	1.07	1.09	0.94	–0.90	0.93
1200S250-97-DFM-1	26885		16	–	18	2075	1920	1.00	–	0.88	–	0.93
1200S250-97-DFM-2	28850		16	–	18	2070	1955	1.06	–	0.88	–	0.94
800S250-68-DFC-1	12030	–13405	23	–26	26	545	530	1.17	1.31	0.89	–0.99	0.97
800S250-68-DFC-2	13245	–11175	26	–22	26	540	520	1.25	1.06	1.02	–0.85	0.96
800S250-68-DFM-1	13070		26	–	26	545	525	1.23	–	1.02	–	0.96
800S250-68-DFM-2	12990		26	–	26	550	510	1.21	–	1.02	–	0.93
1000S200-43-LFC-1	6390	–7180	14	–15	23	520	515	1.05	1.19	0.61	–0.67	0.99
1000S200-43-LFC-2	6940	–7425	16	–16	23	525	525	1.13	1.21	0.69	–0.70	1.00
1000S200-43-LFM-1	6705		16	–	23	525	530	1.10	–	0.68	–	1.01
1000S200-43-LFM-2	6555		15	–	23	525	505	1.08	–	0.67	–	0.96
800S200-33-LFC-1	3490	–3325	16	–15	23	245	240	1.09	1.04	0.71	–0.64	0.98
800S200-33-LFC-2	3210	–3475	14	–14	20	255	250	0.96	1.03	0.73	–0.72	0.98
800S200-33-LFM-1	3355		16	–	23	245	245	1.05	–	0.70	–	1.01
800S200-33-LFM-2	3300		15	–	23	245	235	1.01	–	0.66	–	0.97

^a $M_{max}\theta_{Mmax}$ = maximum moment and corresponding rotation; $M_{min}\theta_{Mmin}$ = minimum moment and corresponding rotation.^b $k_e = 6EI_x / (3L_u + 2a)$, the initial elastic stiffness; k = measured initial stiffness $\theta_y = M_y/k_e$, the yielding rotation.^c Values between parentheses are calculated using Eurocode-3 [42]**Table 6**

Test-to-predicted statistics.

Specimen Group	M_{max}/M_n		M_{min}/M_n		θ_{Mmax}/θ_y		θ_{Mmin}/θ_y		k/k_e	
	μ	COV	μ	COV	μ	COV	μ	COV	μ	COV
Global	0.70	0.04	0.68	0.03	0.49	0.06	0.46	0.11	0.93	0.04
	(0.94)		(0.92)							
Distortional	1.13	0.09	1.13	0.11	0.95	0.07	0.90	0.07	0.95	0.02
Local	1.06	0.05	1.12	0.08	0.68	0.05	0.68	0.05	0.99	0.02
L & D	1.09	0.08	1.12	0.09	0.81	0.18	0.79	0.18	0.97	0.03
Cyclic	0.96	0.22	0.98	0.24	0.70	0.30	0.68	0.28	0.96	0.04
Monotonic	0.96	0.21	–	–	0.71	0.28	–	–	0.95	0.04
All Spec.	0.96	0.21	0.98	0.24	0.71	0.28	0.68	0.28	0.95	0.04

(a) μ = mean value; COV = coefficient of variation; L&D = Local and Distortional.(b) Values between parentheses are calculated using M_n from Eurocode-3 [42].

3.3. Flexural members experiencing distortional buckling (DFM)

Specimens in group 8DFM exhibited distortional buckling of the top flange and top portion of the web with three half-waves similar to those shown in Fig. 8b. Once the maximum moment strength, M_{max} , was reached, the top flange failed locally and strength dropped almost instantly to 65% the peak moment. Inelastic strains accumulated around the failed cross-section and the section folded into itself as deformations increased. Out-of-plane deformations related to lateral-torsional buckling were not observed and no hinges formed at the loading points.

Distortional buckling specimens in group 12DFM experienced buckling of the top portion of the web and flanges with four half-waves as seen in Fig. 8b. The top flange failed locally at the maximum strength, M_{max} , and strength dropped almost instantly to 75% of the peak moment (Fig. 7). The post-peak behavior resembled lateral-torsional buckling with large out-of-plane deformation. Inelastic deformations developed close to the loading

points as additional hinges formed in the later stages of the test with strength degrading to values around $0.3M_y$.

3.4. Flexural members experiencing local buckling (LFM)

Local buckling specimens 8LFM showed buckling of the top portion of the web with 14 half-waves before reaching the maximum flexural strength, M_{max} . At peak moment, the top part of the web close to the junction with the flange yielded and the mid cross-section buckled (Fig. 8c) accompanied by a sudden strength drop, to 50% of the peak moment. The strength then degraded slowly and stabilized around $0.2M_y$ (Fig. 7). After the mid-span cross-section buckled, the response resembled lateral-torsional buckling. Inelastic deformation developed close to the loading points in the later stages of the test.

Local buckling specimens 10LMF buckled with about eight half-waves at the top portion of the web in the early cycles, and this quickly changed to distortional buckling with four half-waves in the top flange before the maximum flexural strength M_{max} . These members had top flange stiffening lips shorter than the nominal values (10.2 mm measured as compared to nominal 15.8 mm). Because of these shorter lips, the average predicted strength by DSM for distortional buckling, $M_{nd} = 6096$ kN-mm, was less than predicted strength for local buckling, $M_{ne} = 6624$ kN-mm, which was also reflected in the observed buckling mode. At peak moment, the top flange locally buckled and strength dropped almost instantly to 65% of M_{max} . The post-peak behavior resembled the behavior of the 8LMF members with large deformations and gradual strength degradation to values around $0.2M_y$.

3.5. Cyclic flexural response

For all cyclic tests, the moment-rotation response started as linear elastic past the first six cycles with similar stiffness in both loading directions (see, Figs. 9a, 11a, and 13a). Buckling

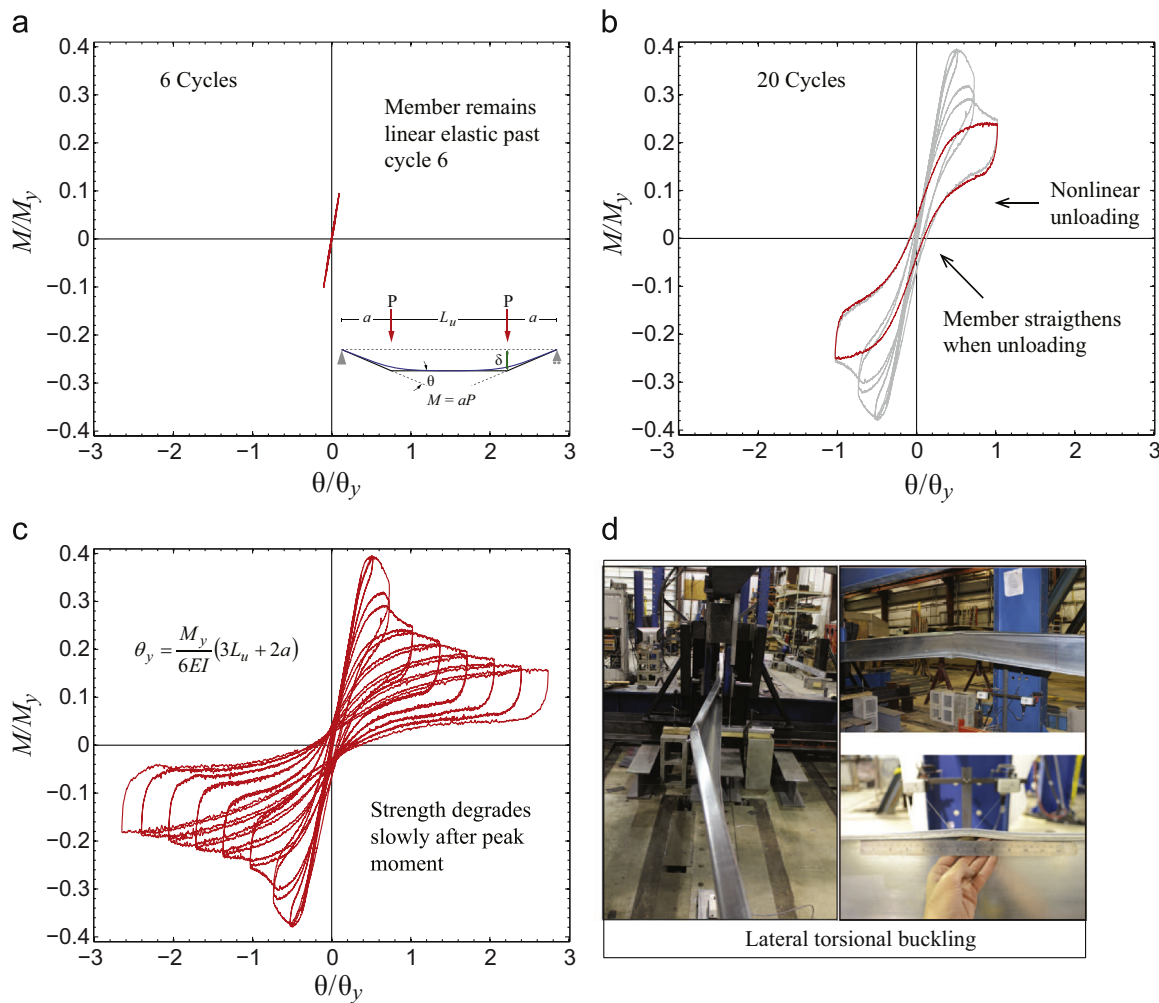


Fig. 9. Cyclic moment-rotation response for specimen 800S162-97-GFC-2 at: (a) 6 cycles, (b) 20 cycles, (c) complete response, (d) failure mode.

deformations typically started after cycle 10 in a pattern similar to the monotonic members and as illustrated in Figs. 9,11, and 13. Specimens generally buckled at different locations during positive and negative flexure due to strain hardening and redistribution of stresses around the first buckled cross-section. Despite this, the cyclic moment-rotation response was symmetric for most of the members with three exceptions described in the following sections. The average ratio of test peak moment to predicted moment for cyclic tests was 0.96 (COV=0.22) and 0.98 (COV=0.24) for positive and negative moment respectively.

3.6. Flexural members experiencing global buckling (GFC)

Global buckling members subjected to cyclic loading (GFC) exhibited lateral-torsional buckling similar to their monotonic counterparts as illustrated in Fig. 9d. Strength decreased rapidly after the peak to about 65% M_{max} , then continued to degrade slowly. The moment-rotation response stabilized around $0.2M_y$ for both cross-section types, which could have implications in seismic design with regards to residual load-carrying capacity, see Fig. 9c. Even though the flanges have buckled and are not contributing to the flexural-torsional stiffness, the members are still able to sustain moment at large deformations because of redistribution of the stresses towards the loading supports through the web and web-flange intersections. Pinching of the response (Fig. 9b) occurred because upon unloading, the member straightened out (towards

the unbuckled initial position) before starting to load in the opposite direction. Damage due to inelastic strains accumulated at the buckled flanges close to the stiffening lips which led to tearing during later cycles. This tearing did not propagate to the flanges. Cyclic strength degradation is minimal when comparing monotonic cyclic responses in Fig. 10.

3.7. Flexural members experiencing distortional buckling (DFC)

Distortional members (DFC) showed buckling of the top flange and top portion of the web similar to their monotonic counterparts as illustrated in Fig. 11d. Moment strength dropped almost instantly after the peak moment to about 60% and 70% of the peak for the 8DFC and 12DFC members respectively. Cyclic strength degradation occurred as damage accumulated at the buckled flanges as evidenced by the gap between the monotonic curves and cyclic envelopes in Fig. 12. Stiffness degraded with every cycle as well. Slight pinching of the hysteretic response occurred as the buckled flange straightened out during load reversal (Fig. 11b). The 12DFC members moment response was symmetric where top and bottom flanges buckled at the mid-span cross-section and subsequent large deformations occurred while sustaining moments around $0.2M_y$ (Fig. 11c). Damage also accumulated close to the loading points for the 12DFC as hinges formed in the last cycles creating a shape resembling lateral-torsional-buckling. The response of the 8DFC members was slightly asymmetric because

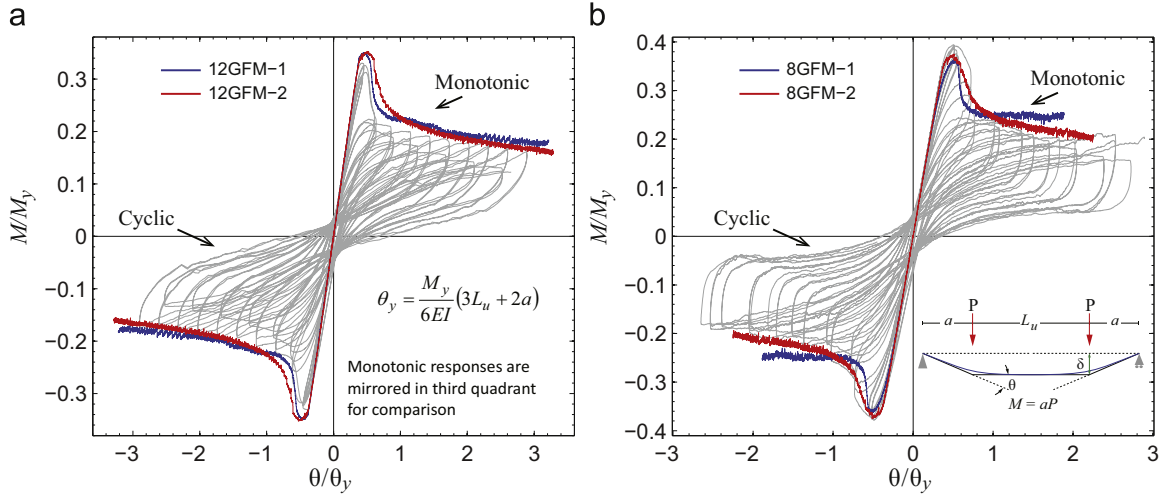


Fig. 10. Global buckling monotonic response envelope: (a) 12 series, (b) 8 series. Cyclic strength degradation is minimal when comparing monotonic cyclic responses.

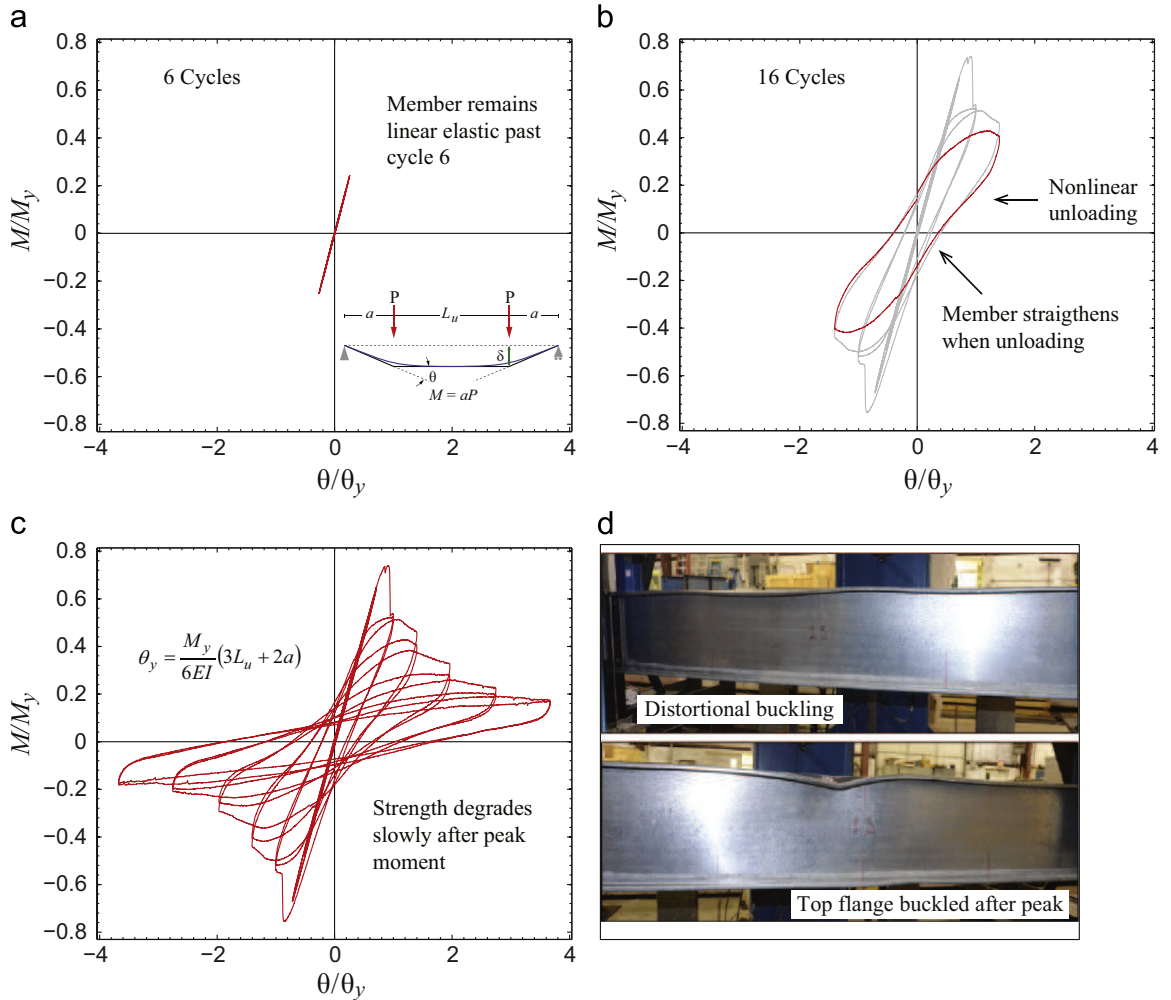


Fig. 11. Cyclic moment-rotation response specimen for 1200S250-97-DFC-1 at: (a) 6 cycles, (b) 16 cycles, (c) complete response, (d) failure mode.

buckling occurred at two different locations, the mid-span cross-section in positive moment and close to the loading point in negative moment. This ultimately affected their post-peak behavior which consisted of folding of the buckled cross-sections without formation of additional hinges.

3.8. Flexural members experiencing local buckling (LFC)

Local members (8LFC) buckled similar to their monotonic counterparts as illustrated in Fig. 13d. Strength dropped almost instantly after the peak moment to about 40% of M_{max} , then degraded as the inelastic deformations accumulated at the top part

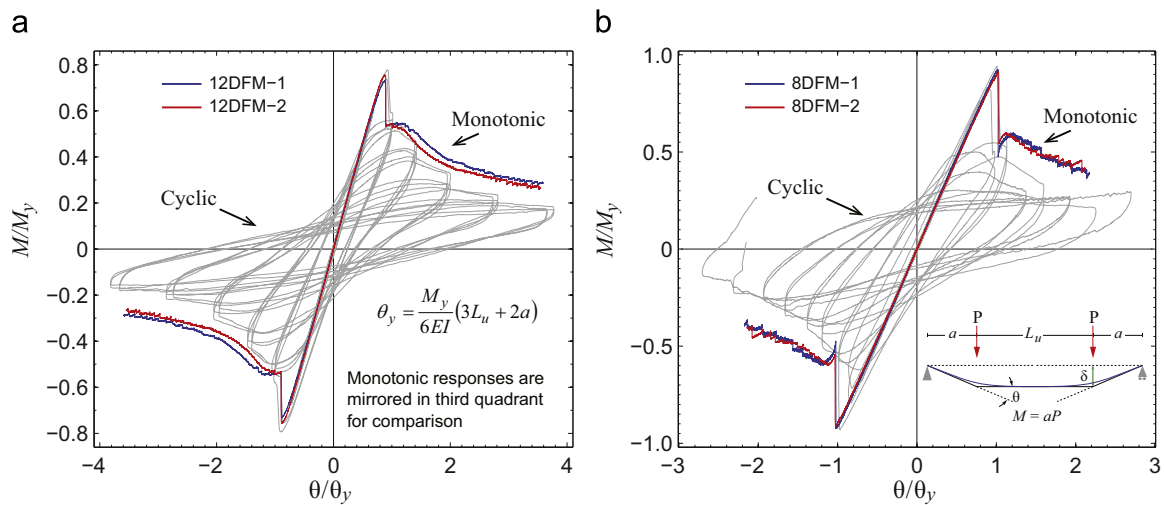


Fig. 12. Distortional buckling monotonic response envelope: (a) 12 series, (b) 8 series. Cyclic strength deterioration at the end of test is around 56% and 64% of the corresponding strength under monotonic loading for 8DFC and 12DFC specimens respectively.

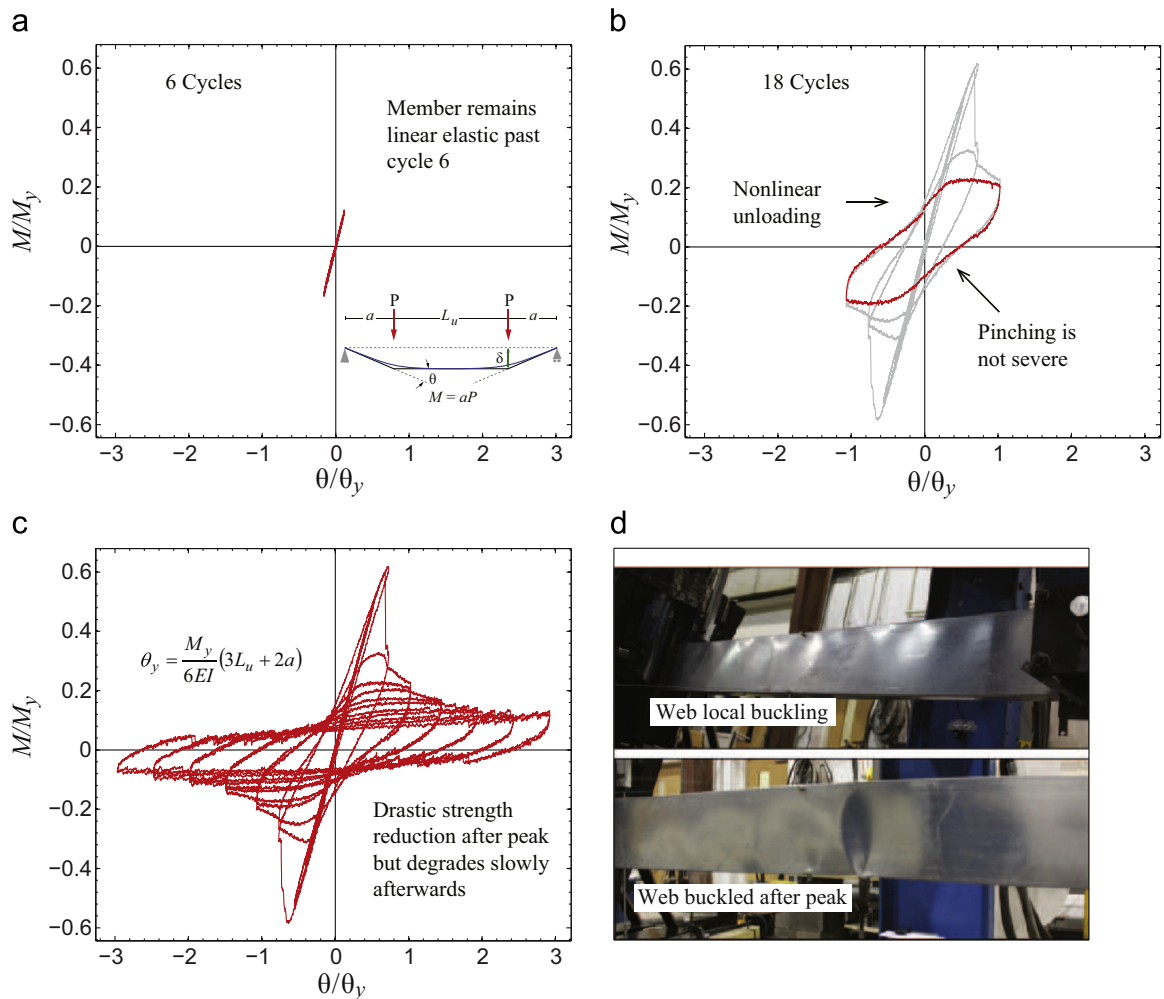


Fig. 13. Cyclic moment-rotation response specimen for 800S200-33-LFC-1 at: (a) 6 cycles, (b) 18 cycles, (c) complete response, (d) failure mode.

of the web close to the web-flange junction. Slight pinching of the hysteretic response occurred as the member straightened during load reversal (Fig. 13b). The response of the 8LFC-1 member was symmetric where web buckling occurred at the mid-span followed by large deformations while carrying moments around $0.1M_y$

(Fig. 13c). Damage also accumulated close to one of the loading points for this member. The response of member 8LFC-2 shown in Fig. 14b, was similar to 8LFC-1 however, the cross-section at the only hinge folded into itself as post-peak deformations increased, providing stiffness and strength gains in both directions during the

last cycles.

Local members 10LFC exhibited local web buckling before peak load that quickly shifted to a distortional buckling pattern similar to their monotonic counterparts. These members also had stiffening lips shorter than the nominal values (10.3 mm measured as compared to nominal 15.8 mm). Strength dropped nearly instantaneously after the peak moment to about 55% of M_{max} and then degraded as damage accumulated at the mid span and in later cycles close to the loading points. The response of specimen 10LFC-2 was asymmetric because of the different directions that the out-of-plane deformations formed in positive and negative moment. The out-of-plane deformations in the positive moment direction favored higher strengths because of compatibility-based membrane tension stiffening. This stiffening effect was not present in the negative moment direction because the bottom flange buckled close to the loading supports forming additional hinges.

3.9. Moment-rotation response comparisons

Comparing the hysteretic response across limit states is challenging because of the different cross-sections, specimen lengths, and buckling failure modes considered in this study. The amount of strength degradation, stiffness degradation, and pinching of the hysteretic response varies for the different specimens; however, if one compares normalized cyclic response envelopes, similar characteristics can be observed across the different buckling modes, unbraced lengths and cross-sections considered.

Cyclic response envelopes were normalized to the respective yield rotation, $\theta_y = \delta_y/a$, and yield moment, M_y , as shown in Fig. 15. It can be seen that the average slope k/k_e for all envelopes is 0.96 (COV=0.04) between peak positive and negative moments, and it demonstrates that the pre-peak stiffness is well characterized by $k_e = 6EI/[3L_u + 2a]$ (see Tables 5 and 6). Strength decreased after the peak moment by at least 35%, and then degraded at different rates as the flexural deformation, θ/θ_y , increased. All specimens had some residual load carrying capacity, on average 0.2 M_y , in both loading directions after sustaining large flexural deformations ($\theta/\theta_y \geq 2$). This result could be useful in characterizing post-peak behavior in seismic design and collapse analysis of CFS structures.

The differences observed between the moment-rotation responses associated with different buckling modes relate to the amount of stiffness degradation and pinching. There is less stiffness degradation and pinching of the hysteretic response for distortional (Fig. 11b) and local buckling (Fig. 13b) members than for

global buckling members (Fig. 9b). This difference correlates to the failure mechanism in global buckling members, which involves inelastic local buckling deformations at the compression lip-flange accompanied by large twist plus lateral deflections at the mid-span cross-section. Accumulation of inelastic deformations at the compression lip-flange every cycle amplifies second-order effects that increase twist and lateral deflections and decrease flexural stiffness. Straightening upon unloading of the increasing large torsional deformations translates into more pinching of the moment-rotation response.

3.10. Energy Dissipation of Cold-Formed Steel Flexural Members

Energy dissipation characteristics in global buckling specimens were different than that of local and distortional buckling specimens. Fig. 16 compares the normalized energy dissipated per cycle (NHE_{pc}) as a function of the cumulative flexural deformation $\Sigma\theta/\theta_y$. The energy dissipated in each cycle, E_{ci} , is normalized to the area of the rectangle, E_{cr} , bounded by the maximum and minimum flexural deformation experienced in that cycle and the predicted moment strength, M_n (see inset in Fig. 16). Global buckling

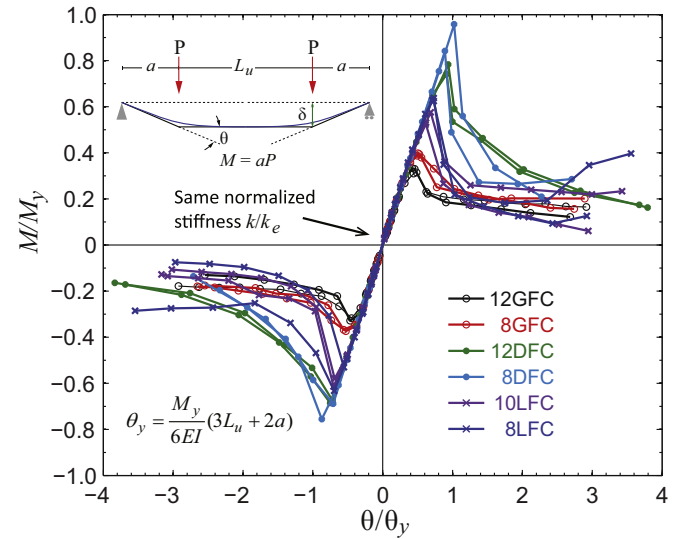


Fig. 15. Cyclic $M-\theta$ response envelopes show post-peak strengths dropping at least 35% of peak moments where local and distortional buckling specimens experience less strength degradation when compared to global buckling specimens.

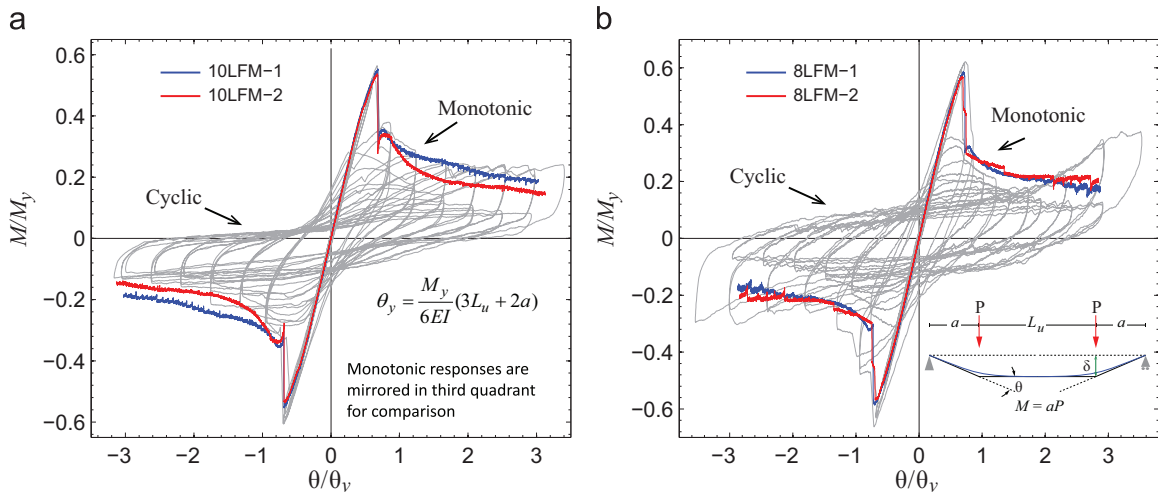


Fig. 14. Local buckling monotonic response envelope, (a) 10 series, (b) 8 series. Strength degrades no more than 40% the corresponding strength under monotonic loading for both 10LFC and 8LFC specimens.

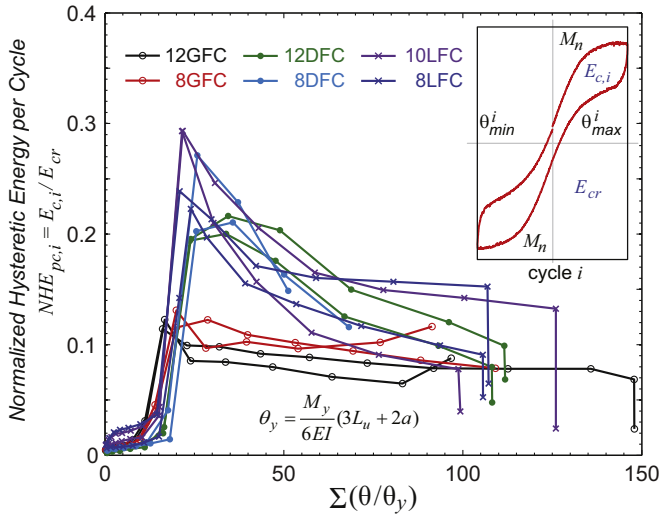


Fig. 16. Normalized energy dissipated per cycle (NHE_{pc}) is less and remains relatively constant in global buckling specimens compared to local and distortional buckling members as cumulative flexural deformations $\Sigma\theta/\theta_y$ increase.

members (GFC) dissipated less energy every cycle than local or distortional members. The amount of pinching of the moment-rotation response, which was more pronounced in the GFC specimens, translated to less energy dissipated per cycle. However, energy dissipation capabilities for the GFC specimens remained relatively constant ($NHE_{pc} \approx 0.1$) with increasing flexural deformations. Conversely, energy dissipation capabilities in local and distortional buckling members reached higher NHE_{pc} values (≥ 0.2) compared to global buckling specimens, and decreased rapidly as flexural deformations increased (see Fig. 16).

The observed differences between global buckling specimens and local and distortional buckling specimens are related to the failure mechanism and how damage accumulated after peak moment at the failed cross-sections and along the unbraced length. Damage in global buckling members was concentrated in the buckled flanges at the mid-span for most of the cycles and close to the loading points at the final cycles when additional hinges formed. In local and distortional buckling specimens, damage initially accumulated at the compression portion of the cross section

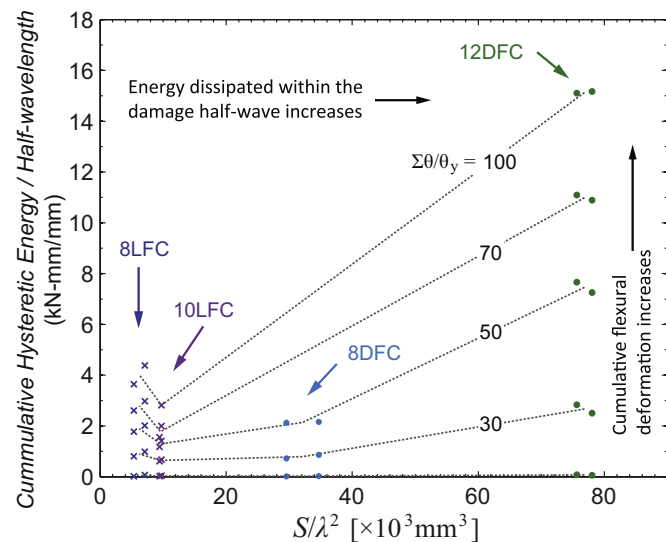


Fig. 17. Cumulative energy dissipated in the damaged half-wave(s) (HE_{pc}/L_{cr}) increases as a function of the section modulus S and cross-section slenderness λ for local and distortional buckling specimens.

(web/flange) and quickly spread across the cross section creating yield lines with folding during every cycle. Because in global buckling members, damage did not spread to the web and folding was absent, the energy dissipation capabilities remained relatively constant.

Energy dissipation (per cycle and cumulative) within the damage half-wave decreases for higher cross-sectional slenderness (λ_d and λ_e) and increases with the cross-section elastic modulus S as shown in Fig. 17 and Table 7. A convenient representation for these trends is to compare S/λ^2 at different cumulative flexural deformations $\Sigma\theta/\theta_y$. Energy dissipation is higher for specimens with small slenderness and large section elastic modulus compared to specimens with larger λ or smaller section modulus S . For instance, 12DFC specimens have the largest S/λ^2 ($= 76.9 \times 10^3 \text{ mm}^3$) values with average cumulative energy dissipated 7.45 kN-mm/mm compared to 1.29 kN-mm/mm of the 10LFC specimens ($S/\lambda^2 = 9.58 \times 10^3 \text{ mm}^3$) for the same cumulative deformation $\Sigma\theta/\theta_y = 50$ (see Table 7). The inversely proportional relationship between energy dissipation and cross-sectional slenderness described is consistent with results from cyclic loaded cold-formed steel axial members observed in [23]. In the case of specimens where damage accumulated at more than one location, energy dissipation remained relatively unaffected despite having the similar slenderness and S/λ^2 values. For example, damage accumulated at two locations in specimen 8LFC-1 but dissipated less energy compared to specimen 8LFC-2 where damage accumulated at only one location close to the mid-span (see Table 7). Because there is higher rotation demand in a member with a single hinge (compared to two), plastic strains accumulation is higher, which translates into more energy dissipated. The 10LFC specimens behavior at peak load was controlled by distortional buckling, therefore the respective L_{crd} and λ_d were used in the normalizations shown in Fig. 17.

The tests discussed in this research were performed with braced shear span a and unbraced constant moment region L_u selected such that buckling and plastic deformations occurred in the constant moment region. For flexural members with moment gradients, the distribution will influence the energy dissipation and the cumulative flexural deformations. Additional tests (or simulations) with moment gradients would certainly reveal the effects of the moment distribution on both of these quantities. These additional tests could be compared to those described herein by using the moment gradient factor C_b and factor β (for global and distortional buckling respectively) from the AISI-S100-12 specifications [37], when calculating the buckling moments M_{cr} and slenderness λ .

4. Conclusion

An experimental program was conducted to investigate the cyclic flexural behavior of cold-formed steel members experiencing local, distortional, and lateral-torsional buckling. Cold-formed steel flexural members can dissipate energy and provide post-buckling strength and stiffness even though the flanges and/or web have buckled because of redistribution of stresses to regions next to the damaged half-wave(s). Flexural strength decreased rapidly after peak moment but some residual load carrying capacity remained, on average $0.2 M_y$, while sustaining large deformations ($\theta/\theta_y > 2$).

Cyclic strength degradation, cyclic stiffness degradation, and pinching of the hysteretic response varied across the different buckling modes. The unloading and reloading mechanisms affected the amount of pinching observed, which was larger in members experiencing lateral-torsional buckling and reflected in the lowest energy dissipation compared to those members experiencing local and distortional buckling.

Table 7
Cumulative hysteretic energy magnitudes.

Specimen	λ	S/λ^2 ($\times 10^{-3} \text{ mm}^3$)	HE_{10}	HE_{20}	HE_{40} (kN-mm)	HE_{80}	HE_T	HE_{10}/L_{cr}	HE_{20}/L_{cr}	HE_{40}/L_{cr} (kN-mm/mm)	HE_{80}/L_{cr}	HE_T/L_{cr}	$\max \Sigma \theta/\theta_y$
1200S162-97-GFC-1	1.45	34.66	306	982	1639	2255	4258	0.201	0.644	1.075	1.479	2.794	148
1200S162-97-GFC-2	1.46	34.11	296	879	1443	1960	2497	0.194	0.577	0.947	1.286	1.639	97
800S162-97-GFC-1	1.33	22.13	276	965	1622	2279	2811	0.181	0.633	1.064	1.495	1.845	91
800S162-97-GFC-2	1.34	21.73	238	939	1630	2291	3196	0.156	0.616	1.070	1.503	2.097	109
1200S250-97-DFC-1	1.11	75.64	165	2003	3550	4690	6038	0.439	5.322	9.431	12.458	16.041	108
1200S250-97-DFC-2	1.09	78.07	132	1781	3337	4518	6098	0.360	4.856	9.097	12.318	16.625	112
800S250-68-DFC-1	1.12	29.56	56	1212	2177	–	2537	0.068	1.476	2.652	–	3.091	68
800S250-68-DFC-2	1.03	34.71	126	1413	–	–	2019	0.140	1.567	–	–	2.238	51
1000S200-43-LFC-1	1.74	9.42	135	677	1004	1251	1460	0.186	0.932	1.382	1.723	2.010	99
1000S200-43-LFC-2	1.71	9.74	150	774	1254	1663	2530	0.206	1.061	1.719	2.280	3.469	126
800S200-33-LFC-1	1.76	5.36	37	289	482	649	835	0.169	1.322	2.206	2.972	3.824	106
800S200-33-LFC-2	1.57	7.11	76	330	546	755	1028	0.352	1.517	2.511	3.473	4.727	107

HE_{xx} =cumulative hysteretic energy dissipated up to $\Sigma \theta/\theta_y = xx$; HE_T =cumulative hysteretic energy dissipated end of test; $\max(\Sigma \theta/\theta_y)$ =cumulative deformation at the end of the test; λ =governing slenderness from Table 3; S =cross-section elastic modulus.

Energy was dissipated through inelastic strains and cold-bending at the buckled cross-section(s), and varied depending on the buckling mode as well as the number of locations where damage accumulated along the unbraced length. Energy dissipation capabilities remained constant for members experiencing lateral-torsional buckling while enduring large deformations. Members experiencing local and distortional buckling dissipated more energy per cycle than members experiencing lateral-torsional buckling, but the dissipation capabilities rapidly decreased as flexural deformations increased. When damage accumulated at more than one location along the unbraced length (i.e., two flexural hinges), the cumulative energy dissipated was less compared to members with similar slenderness that only exhibited one flexural hinge. Higher rotation demand in a member with a single hinge, translates into more plastic strains accumulation and more energy dissipation.

A key observation was that energy dissipation within a damaged half-wave for local and distortional buckling decreases with increasing cross-sectional slenderness (λ_d and λ_r) and increases with the cross-section elastic modulus S . Work is ongoing to adapt these results to nonlinear hysteretic models for CFS flexural members for use in computational simulation and analysis-based seismic design.

Acknowledgements

The authors are grateful to the American Iron and Steel Institute (AISI) for supporting this project; to the AISI Project Monitoring Task Group especially Bonnie Manley, Ben Schafer, Jay Larson, Colin Rogers, Steve Tipping; and to Greg Ralph and Ken Curtis at Clark Dietrich Building Systems for the specimen donations.

References

- [1] J. DaBreio, N. Balh, C. Ong-Tone, C.A. Rogers, Steel sheathed cold-formed steel framed shear walls subjected to lateral and gravity loading, *Thin-Walled Structures* 74 (2014) 232–245.
- [2] N. Balh, J. DaBreio, C. Ong-Tone, K. El-Saloussy, C. Yu, C.A. Rogers, Design of steel sheathed cold-formed steel framed shear walls, *Thin-Walled Structures* 75 (2014) 76–86.
- [3] M. Zeynalian, H. Ronagh, Experimental Study on Seismic Performance of Strap-Braced Cold-Formed Steel Shear Walls, *Advances in Structural Engineering* 16 (2013) 245–258.
- [4] I. Shamim, C.A. Rogers, Steel sheathed/CFS framed shear walls under dynamic loading: Numerical modelling and calibration, *Thin-Walled Structures* 71 (2013) 57–71.
- [5] I. Shamim, J. DaBreio, C.A. Rogers, Dynamic Testing of Single- and Double-Story Steel-Sheathed Cold-Formed Steel-Framed Shear Walls, *Journal of Structural Engineering* 139 (2013) 807–817.
- [6] Yu C, Li C. Behavior and strength of cold-formed steel framed shear walls sheathed with composite panels. 21st International Specialty Conference on Cold-Formed Steel Structures, October 24–25, 2012, Center for Cold-Formed Steel Structures, p. 637–651.
- [7] Yu C, Li C. Experimental investigation of cold-formed steel shear walls sheathed with steel-gypsum composite panels. Structural Stability Research Council Annual Stability Conference, April 18–21, 2012, Structural Stability Research Council (SSRC), p. 298–309.
- [8] M. Nithyadharan, V. Kalyanaraman, Behaviour of cold-formed steel shear wall panels under monotonic and reversed cyclic loading, *Thin-Walled Structures* 60 (2012) 12–23.
- [9] Q. Peck, N. Rogers, R. Serrette, Cold-Formed Steel Framed Gypsum Shear Walls: In-Plane Response, *Journal of Structural Engineering* 138 (2012) 932–941.
- [10] Liu P, Peterman KD, Yu C, Schafer BW. Cold-formed steel shear walls in ledger-framed buildings. Structural Stability Research Council Annual Stability Conference, April 18–21, 2012, Structural Stability Research Council (SSRC); 2012, p. 310–323.
- [11] Liu P, Peterman KD, Yu C, Schafer BW. Characterization of cold-formed steel shear wall behavior under cyclic loading for the CFS-NEES building. 21st International Specialty Conference on Cold-Formed Steel Structures, October 24–25, 2012, Center for Cold-Formed Steel Structures, p. 703–722.
- [12] Dastjerdi MZ, Ronagh HR. Seismic performance of steel sheathed cold-formed steel shear walls. 21st International Specialty Conference on Cold-Formed Steel Structures, October 24–25, 2012, Center for Cold-Formed Steel Structures, p. 671–685.
- [13] Schafer BW, Ayhan D, Leng J, Liu P, Padilla-Llano DA, Peterman KD, Stehman M, Buonopane SG, Eatherton MR, Madsen RL, Manley B, Moen CD, Nakata N, Rogers CA, Yu C. “The CFS-NEES Effort: Advancing Cold-Formed Steel Earthquake Engineering,” 10th U.S. National Conference on Earthquake Engineering, July 21–25, 2014, Anchorage, AK.
- [14] K.D. Peterman, N. Nakata, B.W. Schafer, Hysteretic characterization of cold-formed steel stud-to-sheathing connections, *Journal of Constructional Steel Research* 101 (2014) 254–264.
- [15] A. Okasha, Performance of steel frame/wood sheathing screw connections subjected to monotonic and cyclic loading, University of McGill, 2004, M.Sc. Thesis.
- [16] Ayhan D, Schafer BW. Characterization of moment-rotation response of cold-formed steel beams. Proceedings of the Annual Stability Conference, SSRC, April 18–21, 2012, Grapevine, Texas.
- [17] Madsen RL, Nakata, N, Schafer BW, “CFS-NEES Building Structural Design Narrative”, Research Report, RR01, access at www.ce.jhu.edu/cfsnees, October 2011, revised RR01c May 2012.
- [18] Peterman KD, Stehman M, Buonopane SG, Nakata N, Madsen RL, Schafer BW. Stability behavior of full-scale cold-formed steel buildings under seismic excitations. Structural Stability Research Council Annual Stability Conference 2014, SSRC 2014, March 25–28, 2014.
- [19] K.D. Peterman, Behavior of full-scale cold-formed steel buildings under seismic excitations, Johns Hopkins University, Baltimore, 2014, Ph.D. dissertation.
- [20] AISI S213-07, North American Standard for Cold-Formed Steel Framing: Lateral Design, American Iron and Steel Institute, Washington, D.C., 2007, ANSI/AISI-S213-07.
- [21] FEMA, FEMA P695-Quantification of Building Seismic Performance Factors, Federal Emergency Management Agency (FEMA), Washington, D.C. 2009, Document No. FEMA 965.
- [22] Padilla-Llano DA, Moen CD, Eatherton MR. “Cyclic flexural hysteretic models for cold-formed steel seismic simulation”. 7th European Conference on Steel and Composite Structures, Eurosteel 2014, September 10–12, 2014.
- [23] D.A. Padilla-Llano, C.D. Moen, M.R. Eatherton, Cyclic axial response and energy dissipation of cold-formed steel framing members, *Thin-Walled Structures* 78 (2014) 95–107.

- [24] M. Wong, K. Chung, Structural behaviour of bolted moment connections in cold-formed steel beam-column sub-frames, *Journal of Constructional Steel Research* 58 (2002) 253–274.
- [25] C.-M. Uang, A. Sato, J.-K. Hong, K. Wood, Cyclic testing and modeling of cold-formed steel special bolted moment frame connections, *Journal of Structural Engineering* 136 (2010) 953–960.
- [26] A. Bagheri Sabbagh, M. Petkovski, K. Pilakoutas, R. Mirghaderi, Experimental work on cold-formed steel elements for earthquake resilient moment frame buildings, *Engineering Structures* 42 (2012) 371–386.
- [27] S. Yin, Corona E, Ellison M. Degradation and Buckling of I-Beams under Cyclic Pure Bending, *Journal of Engineering Mechanics* 130 (2004) 809–817.
- [28] G.C. Lee, E.T. Lee, Local buckling of steel sections under cyclic loading, *Journal of Constructional Steel Research* 29 (1994) 55–70.
- [29] H.-L. Hsu, P.-S. Chi, Flexural performance of symmetrical cold-formed thin-walled members under monotonic and cyclic loading, *Thin-Walled Structures* 41 (2003) 47–67.
- [30] M. Elchalakani, X. Zhao, R. Grzebieta, Cyclic Bending Tests to Determine Fully Ductile Section Slenderness Limits for Cold-Formed Circular Hollow Sections, *Journal of Structural Engineering* 130 (2004) 1001–1010.
- [31] P.K. Shaw, S. Kyriakides, Inelastic analysis of thin-walled tubes under cyclic bending, *International Journal of Solids and Structures* 21 (1985) 1073–1100.
- [32] S. Kyriakides, P.K. Shaw, Inelastic Buckling of Tubes Under Cyclic Bending, *J Pressure Vessel Technol* 109 (1987) 169–178.
- [33] S.P. Vaze, Corona E. Degradation and collapse of square tubes under cyclic bending, *Thin-Walled Structures* 31 (1998) 325–341.
- [34] B. Calderoni, A. De Martino, A. Formisano, L. Fiorino, Cold formed steel beams under monotonic and cyclic loading: Experimental investigation, *Journal of Constructional Steel Research* 65 (2009) 219–227.
- [35] B. Calderoni, C. Giubileo, A. De Martino, Assessment of hysteretic cyclic behaviour of plastic hinge in cold-formed steel beams. 5th International Conference on Behaviour of Steel Structures in Seismic Areas-Stessa 2006, August 14, 2006–August 17, 2006, Taylor and Francis/Balkema (2006), p. 185–190.
- [36] A. De Martino, A. Formisano, B. Calderoni, Flexural cyclic behaviour and low-cycle fatigue of cold-formed steel members, in: H. Koukari, L. Bragança, H. Trumpf, G. de Matteis, F. Mazzolani, C. Schaur, J.P. Jaspart, G. Huber (Eds.), *Improvement of Buildings' Structural Quality by New Technologies*, Taylor & Francis, 2005, pp. 301–309.
- [37] AISI-S100-12, North American Specification for the Design of Cold-Formed Steel Structural Members, American Iron and Steel Institute, Washington, D.C., 2012, ANSI/AISI-S100-S112.
- [38] SSMA Steel Stud Manufacturers Association, Product Technical Information, ICBO ER-4943P, (<http://www.ssmacom>), December 15, 2011.
- [39] C.D. Moen, Direct strength design for cold-formed steel members with perforations, Johns Hopkins University, Baltimore, 2008, Ph.D. dissertation.
- [40] B.W. Schafer, S. Adany, Buckling analysis of cold-formed steel members using CUFSM: conventional and constrained finite strip methods. In: *Proceedings of the 18th international specialty conference on cold-formed steel structures*, University of Missouri-Rolla, Orlando, FL, United states, 2006.
- [41] ASTM. E8M-13a, Standard Test Methods for Tension Testing of Metallic Materials (Metric), ASTM International, West Conshohocken, PA, 2013.
- [42] EN-1993. Eurocode 3: design of steel structures. European Committee for Standardization. Brussels, Belgium; 2006.
- [43] P.D. Moncarz, H. Krawinkler, Theory and Application of Experimental Model Analysis in Earthquake Engineering, The John A. Blume Earthquake Engineering Center Report No. 50 (1981).
- [44] AISI-S911-08, Method for Testing Cold-Formed Steel Hat Shaped Beams, American Iron and Steel Institute, Washington, D.C., 2008, ANSI/AISI-S911-08.
- [45] FEMA, FEMA 461-Interim protocols for determining seismic performance characteristics of structural and nonstructural components through laboratory testing, Federal Emergency Management Agency (FEMA), 2007, Document No. FEMA 461.
- [46] C.D. Moen, B.W. Schafer, Experiments on cold-formed steel columns with holes, *Thin-Walled Structures* 46 (10) (2008) 1164–1182.
- [47] V.M. Zeinoddini, Geometric imperfections in cold-formed steel members, Johns Hopkins University, Baltimore, 2011, Ph.D. dissertation.
- [48] McAnallen LE, Padilla-Llano DA, Zhao X, Moen CD, Schafer BW, Eatherton MR, Initial Geometric Imperfection Measurement and Characterization of Cold-Formed Steel C-Section Structural Members with 3D Non-Contact Measurement Techniques. *Proceedings of the Annual Stability conference*, SSRC 2014, March 25–28, 2014, Toronto, Canada..
- [49] ASTM-C955-09, Standard Specification for Load-Bearing (Transverse and Axial) Steel Studs, Runners (Tracks), and Bracing or Bridging for Screw Application of Gypsum Panel Products and Metal Plaster Bases, West Conshohocken, PA., 2009.
- [50] C.D. Moen, T. Igusa, B.W. Schafer, "Prediction of Residual Stresses and Strains in Cold-Formed Steel Members.", *Thin-Walled Structures* 46 (11) (2008) 1274–1289.
- [51] B.W. Schafer, T. Pekoz, Computational modeling of cold-formed steel: characterizing geometric imperfections and residual stresses, *Journal of Constructional Steel Research* 47 (3) (1998) 193–210.
- [52] Ayhan D and Schafer B.W., Characterization of moment-rotation response of cold-formed steel beams. *Proceedings of the Annual Stability conference*, April 18–21, 2012, Grapevine, Texas.
- [53] VTechWorks, (<http://hdl.handle.net/10919/18721>) (May, 2014).